

A Study of the Orbits and Characteristics of Several Near-Earth Asteroids

Bradley Makinson
L3 Advanced Laboratory
Submitted: April 17, 2024

We present an investigation of the orbital dynamics and physical characteristics of four near-Earth asteroids (NEAs), namely 1998 XB, 2001 QQ142, 1991 AQ, and Toro, alongside a single main-belt asteroid, Dembowska. We use astrometric measurements performed on observations taken from both Durham, UK, and La Palma, Spain, to determine constraints on the orbital parameters for each asteroid via the method of least squares in conjunction with the jackknifing technique. We first use these results to confirm the classification of all five asteroids as either Apollo in the case of 2001 QQ142, 1991 AQ, and Toro, Aten in the case of 1998 XB, or main-belt in the case of Dembowska. We then use the six Keplerian orbital elements for each NEA to determine their distance from Earth as a function of time, from which we estimate their probability of Earth impact via Monte-Carlo techniques. We then proceed to use V-band photometric measurements to estimate the diameter and mass of each NEA by assuming uniform densities from their spectral type and geometric albedos from the literature. A lower bound on the impact energy for each NEA is hence calculated by assuming parallel motion of the Earth and asteroid at the point of impact. From this, we quantify the risk posed by each NEA on the Torino scale, yielding rankings of 0 for all NEAs except 1991 AQ, for which a provision rating of 1 was assigned. It was concluded that whilst this rating indicates that 1991 AQ requires careful monitoring, it would likely be downgraded once additional observations were included in the analysis to reduce the orbital uncertainties. Finally, by applying phase dispersion minimisation to a series of light curve measurements, we determine the synodic rotation period of Dembowska to be 4.68 ± 0.15 hours, which is in good agreement with the available literature. We conclude that, with additional project time, this technique could be successfully applied to NEAs with longer rotation periods.

I. Introduction

The solar system contains a vast number of asteroids, many of which are remnants of collisions during its infancy. Most have settled into stable orbits in the main belt, however a small percentage of these asteroids, known as Near-Earth Asteroids (NEAs), come within close proximity to Earth and, as such, pose a threat to civilisation should an impact occur. Interest in the study of these NEAs has increased significantly in recent times due to events such as the Chelyabinsk event in 2013, where an asteroid 16-19m in size entered Earth's atmosphere over the city of Chelyabinsk in Russia, causing a large fireball and an explosion equivalent to ~ 500 kilotons of TNT (Emel'yanenko et al. 2013). Larger asteroids, such as the ~ 10 km Chicxulub impactor (Chiarenza et al. 2020), have the potential to terminate civilisation on Earth, and it is therefore of paramount importance that the positions of NEAs are accurately tracked in order to determine any significant impact risks in the future. In this work, we assess the risk posed by several NEAs by performing an astrometric and photometric analysis on a series of observations taken from observatories in both Durham, UK, and La Palma, Spain.

The risk posed by NEAs can be quantified by placing them on the Torino scale, which was proposed in 1999 as an analogue to the Richter scale for categorizing the threat posed by newly discovered NEAs (Adams et al. 2004). As shown in Fig. 1, the Torino scale is a colour-coded integer scale from 0 to 10, encapsulating both the likelihood and consequences of a potential collision, where higher values indicate a more significant risk. The asteroid 99942 Apophis was given a provisional rating of 4 - the highest Torino scale ranking to date - for several days after its discovery in 2004 (Bancelin et al. 2012), although this was later downgraded after a larger number of observations were included in the analysis. Nevertheless, this temporary scare provoked significant interest in the risk posed by NEAs, and illustrates the importance of both quantifying this risk on a numerical scale, as well as long observation arcs to provide reliable orbital determinations. It should be noted that the Torino scale does not take into account the

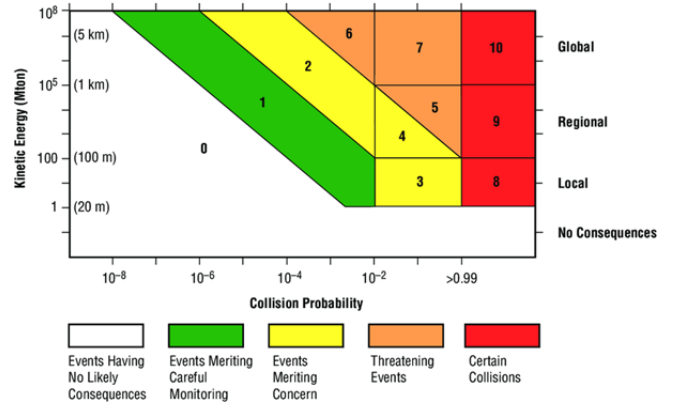


FIG. 1. The Torino Scale used to categorize the risk posed by NEAs (Adams et al. 2004).

time until a potential impact, which is something that one should consider alongside the Torino scale ranking when discussing the threat posed by an NEA.

It is clear that to be able to categorize NEAs on the Torino scale, knowledge of their position relative to Earth is required, which can be derived from the shape and orientation of their orbit. Asteroids follow heliocentric orbits which are elliptical in shape, and therefore can be defined by the six Keplerian orbital elements, along with their epoch of osculation. The six Keplerian orbital elements are the semi-major axis (a) and eccentricity (e), which define the size and shape of the ellipse, the inclination (i) and longitude of the ascending node (Ω), which define the orientation of the orbital plane, and the argument of periapsis (ω) and mean anomaly (M), which define the orientation of the ellipse in the orbital plane and the position of the asteroid at the epoch of osculation, respectively. These parameters are visualised in Fig. 2.

There are certain conditions that a newly-discovered asteroid must satisfy to be considered as an NEA. Two quantities which are used to classify asteroids are the perihelion distance, q , and aphelion distance, Q , which describe the asteroid's closest and furthest distances from the Sun respectively. An asteroid is considered to be an NEA if it satisfies $q \leq 1.3\text{AU}$ or $Q \geq 0.983\text{AU}$ (Birlan et al. 2010). There are several different sub-classes of NEAs

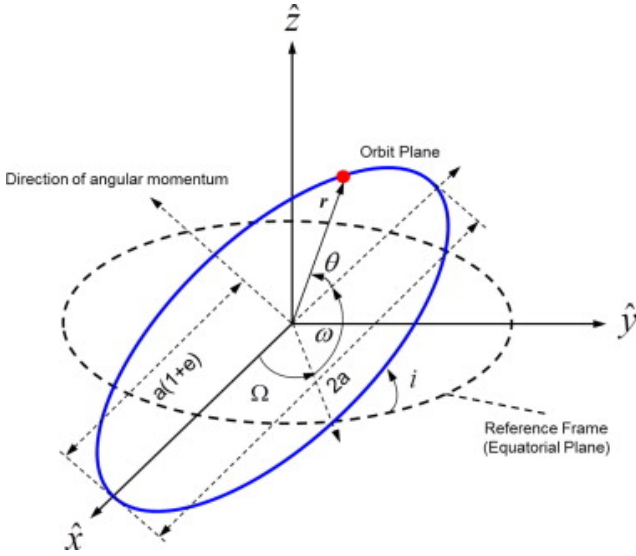


FIG. 2. The six Keplerian elements used to describe the elliptical orbit of an asteroid (Shin et al. 2015).

TABLE I. The classifications and assumed physical characteristics for the asteroids investigated in this report. All albedos are taken from the JPL Horizons system (Giorgini et al. 1996), and all densities are assumed from the spectral type of the asteroid (Krasinsky 2002).

Asteroid	Group	Albedo	Spectral Type (Tholen)	Assumed Density [kg m^{-3}]
Toro	Apollo	0.310	S	2710
1998 XB	Aten	0.489	S	2710
2001 QQ142	Apollo	0.140	S	2710
1991 AQ	Apollo	0.242	Q	2710
Dembowska	Main-belt	0.384	R	2710

which differentiate them based on their orbits relative to that of Earth. Two key sub-classes of NEAs whose orbits cross that of the Earth are the Apollos and Atens. Apollo/Aten asteroids have semi-major axes that are larger/smaller than the Earth's, and hence spend more time outside/inside of the Earth's heliocentric orbit. Hence, Apollo class NEAs satisfy $a > 1$ AU and $q < 1.017$ AU, whilst Aten class NEAs satisfy $a < 1$ AU and $Q > 0.983$ AU. These sub-classes are of particular importance, and hence will be the focus of this report, as it is NEAs which cross the Earth's orbit that pose the greatest risk of impact.

As of April 2024, NASA's CNEOS statistics show that ~ 35000 NEAs are known, of which $\sim 56\%$ are classified as Apollo asteroids, and $\sim 8\%$ are classified as Atens, with this number growing exponentially with time, largely owing to the Pan-STARRS (Kaiser 2004) and Catalina (Christensen et al. 2012) surveys. In this work, we focus on four NEAs, namely Toro, 1998 XB, 2001 QQ142, and 1991 AQ, whose classifications and characteristics are given in Table I. We determine the six Keplerian orbital elements along with the perihelion and aphelion distances for each target NEA (and their uncertainties), along with their impact probabilities and several key physical characteristics, namely diameter, mass, and impact velocity. Knowledge of these physical characteristics and impact probabilities allow us to quantify the threat posed by each NEA by placing them on the Torino scale.

Another key physical quantity for NEAs is their rotational period. Knowledge of the rotational period of NEAs is extremely important as it allows for their

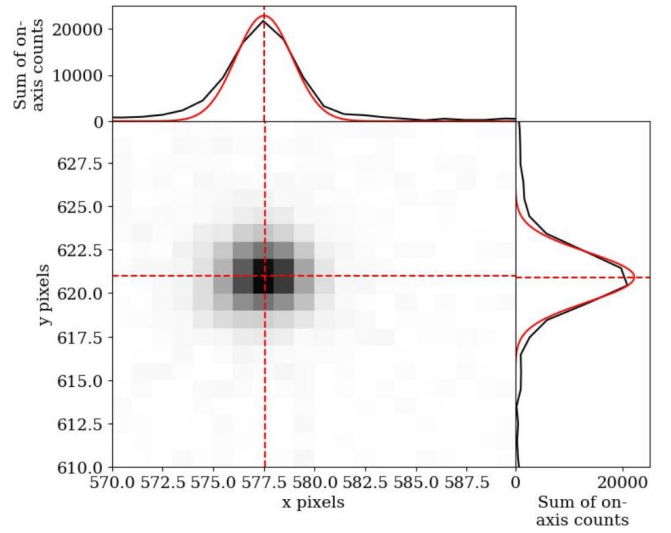


FIG. 3. An illustration the Gaussian fitting process used to determine the position and associated uncertainty of astronomical objects. The main plot shows a cutout of the CCD for an observation of the asteroid Toro, where a darker pixel represents a larger number of counts. The two subplots show the sum of the on axis counts along the x and y directions respectively in black, and the marginalised Gaussian PSFs fitted to the light source in red. A dashed red line is shown to indicate the centroid position of the fitted 2D Gaussian. One can see that the fitted Gaussians correctly model the light profile in both the x and y directions.

morphology and dynamical evolution to be inferred (Lam et al. 2023). Due to tight time constraints, we carry out an analysis of a well-placed, bright, relatively short-period main-belt asteroid, Dembowska, to illustrate how the rotational period of asteroids can be determined via their light curves using the data analysis technique of phase dispersion minimisation.

II. Method and Data Reduction

As outlined in Table I, we investigate five asteroids in this work, each of which were chosen as they were well-placed for the duration of the project, sufficiently bright, and provided a balance between Apollo and Aten NEAs which reflects the statistics given in section I.

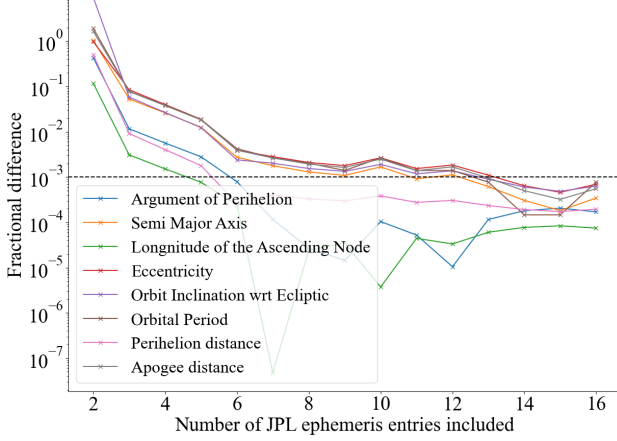
A. Observations

For the duration of this project, we take regular observations of each asteroid whenever the weather permits and the target is visible. As shown from the observation logs provided in appendix A, these observations were taken on a range of dates, spanning from 6th January 2024 to 27th February 2024, providing observation arcs of up to 52 days for all targets. The observation logs also provide information on the exposure times we use for each target, which vary throughout the duration of the project as asteroids are highly dynamical objects whose distance from Earth, and thus apparent magnitude, can vary greatly in a short period of time. We use exposure times which provide a sufficient signal-to-noise ratio such that astrometric and photometric analysis can be carried out, whilst also taking care to ensure that the target does not saturate the CCD.

For each observation night, we take a series of observations of each target, from which the 'best' observation was used for astrometric measurements. We choose the 'best' observation as the one which has

TABLE II. Specifications of the telescopes used to take observations in this work. The latitude and longitude coordinates are taken from the JPL Horizons system.

Telescope	Location	Latitude	Longitude	Diameter	Pixel Scale [arcsec pixel ⁻¹]
West-14	Durham, UK	54.77°	358.42°	35.6 cm	0.91
East-16	Durham, UK	54.77°	358.42°	40.6 cm	0.93
Draco2	Durham, UK	54.77°	358.42°	35.6 cm	0.983
Far-East-20	Durham, UK	54.77°	358.42°	50 cm	1.07
Pt5m	La Palma, Spain	28.76°	342.12°	50 cm	0.28

**FIG. 4.** The fractional difference between the orbital elements returned by *find_orb* and those on the JPL Horizons system as a function of the number of JPL ephemeris entries (1 day separation) passed into *find_orb* for the NEA Toro. The y-axis is shown on a log scale, and a dashed black horizontal line is included at a fractional difference of 10^{-3} . One can see that after 14 entries, a fractional difference of $< 10^{-3}$ is achieved.

a low atmospheric seeing to reduce the Full-Width Half-Maximum (FWHM) of the target source, as well as a large number of stars detected to allow for an accurate astrometric calibration, as will be explained in the following subsection. Additionally, we use a range of telescopes across different observation nights, details for which are given in Table II.

B. Astrometric Measurements

Using the 'best' observations for each asteroid, we measure its position on the sky relative to the stars in the image in an equatorial coordinate system, where the positions of astronomical objects are specified by their Right Ascension (RA) and Declination (Dec). The RA and Dec coordinates are calibrated by fitting a coordinate grid to the stars in the image and minimising the resulting residuals (the difference between where the coordinate grid expects the catalogued stars to be, and where they actually lie). This process results in a systematic error on the measured position of any astronomical object in the image, σ_{sys} , which we take to be the root mean square of the residuals in both the RA and Dec directions.

During an exposure, light from an asteroid is smeared over a distribution of pixels on the CCD due to factors such as atmospheric seeing and telescope vibrations. This distribution of light, called the 'Point Spread Function' (PSF), can be described by a Gaussian distribution. Hence, to determine the RA/Dec coordinates of our target NEAs, we fit a 2D Gaussian PSF to the light distribution on the CCD, with the coordinates at the centroid position being taken as the asteroid's coordinates, as shown in Fig. 3. It is important that exposures do not saturate the CCD as this

would interfere with the Gaussian fitting process, leading to inaccurate results. The random error on these coordinates, σ_{ran} , is related to the the FWHM of the fitted 2D Gaussian along the relevant axis via

$$\sigma_{\text{ran}} = \frac{\text{FWHM}}{2.355 \times \text{SNR}}, \quad (1)$$

where SNR is the asteroid's signal-to-noise ratio, which we determine via aperture photometry using the formula

$$\text{SNR} = \frac{S}{\sqrt{S + n \times (B + T + \sigma_r^2)}}, \quad (2)$$

where S is the number of background-subtracted counts collected from the object, n is the number of pixels within the aperture, and B , T , and σ_r are the mean background count, dark current (which we consider negligible), and read-out noise per pixel (usually ~ 10). It is clear that a lower FWHM and a higher SNR will reduce this contribution to the asteroid's positional uncertainty. However, stacking images to achieve both of these goals was not plausible for the NEAs investigated in this work due to their large proper motion causing significant smearing when separate exposures were stacked.

C. Orbit Determination, Earth-Asteroid Distance, and Impact Probabilities

In this work, we determine orbital elements by passing the set of astrometric measurements for each asteroid into Bill Gray's *find_orb* software (Gray 2022), which determines the asteroid's orbital parameters via the method of least squares, and automatically removes outlying measurements. To investigate the validity of *find_orb*, we pass a varying number of JPL Ephemeris entries with a 1 day separation into *find_orb*, and compare the orbital elements it returns to those on the JPL Horizons system. This is shown graphically in Fig. 4 for the NEA Toro, from which one can see that the fractional difference decreases with an increasing number of JPL ephemeris entries, as expected - a fractional difference of $< 10^{-2}$ is achieved after 6 entries, and $< 10^{-3}$ after 14 entries. One can also see that after 13 entries are used, all orbital elements converge and vary very little with an increasing number of entries beyond this point, providing further confidence that the algorithm is functioning as expected. It should be noted that orbital elements are dynamical quantities, and so can vary in time due to factors such as gravitational interactions. Therefore, whilst this comparison to JPL is a good indicator as to the validity of *find_orb*, the epoch of osculation of the orbital elements returned by *find_orb* will not be identical to the epoch of osculation of those on the JPL Horizons system, so we would not necessarily expect the two sets of orbital elements to be identical. Nevertheless, the fact that the fractional difference decreases with an increasing

number of ephemeris entries, converges, and drops below 10^{-3} provides us with confidence that the algorithm is functioning correctly.

Whilst *find_orb* also returns an estimate for the uncertainty on each orbital element, we instead discern the uncertainties via the 'jackknifing' technique (Sakai et al. 2019), where the orbital elements are repeatedly calculated with one astrometric measurement removed from the set at a time. This process produces an array of values for each orbital parameter, where the mean/standard deviation of each array can be taken as the best-fit value/ 1σ uncertainty on each orbital parameter. For simplicity, we ignore future gravitational interactions between the NEAs and other bodies, meaning we are inherently assuming that the orbital parameters and their uncertainties are constant in time.

Using the derived orbital elements, we determine the position of each NEA in a cartesian heliocentric coordinate system, from which their distance to Earth as a function of time can be calculated. We utilise the PyEphem library in Python to convert the six derived Keplerian orbital elements, along with their epoch of osculation, into heliocentric x , y , and z coordinates at any epoch. We determine these coordinates and their uncertainties via a Monte-Carlo approach - by taking the mean and standard deviation of the positions of 10000 virtual asteroids, each of which is assigned orbital parameters given by randomly sampling normal distributions constructed from the mean and 1σ uncertainty of each orbital element found via jackknifing. A relatively large number of virtual asteroids were chosen to ensure that the positional distributions closely represent a Gaussian, and hence the derived uncertainties are reliable.

The cartesian heliocentric coordinates of each NEA at a given epoch, along with the position of Earth at that epoch (found using the Sun class in PyEphem), can be used to determine the NEA's distance from Earth by adding the difference between the NEA's coordinates and Earth's coordinates in each dimension in quadrature. Using this methodology, we calculate the Earth-asteroid distance for each of the 10000 virtual asteroids as a function of time, with a 1 day separation between points. We then take the mean and standard deviation at each point as the NEA's distance from Earth and associated uncertainty at that time. We also plot cumulative histograms of the closest approach distance and date for the virtual asteroids, to which a cumulative distribution function (CDF) can be fitted, and the NEA's closest approach distance and date can be extracted along with their uncertainties. We extract the probability of Earth impact from this CDF, by finding the cumulative probability of the Earth-asteroid distance being less than one Earth radius.

D. Parallax Measurement

We then proceed to investigate the validity of our methodology by comparing the distances predicted by the above algorithm to those determined via a parallax distance measurement for the NEA Toro using simultaneous observations from Durham and La Palma. The parallax distance, d , can be calculated via

$$d = \frac{B}{2 \sin\left(\frac{\Delta\theta}{2}\right)}, \quad (3)$$

where B is the baseline between Durham and La Palma, and $\Delta\theta$ is the solid angle between the equatorial positions

of Toro as viewed from Durham and La Palma. This solid angle is given by

$$\Delta\theta = \sqrt{(\Delta RA)^2 + (\Delta Dec)^2}, \quad (4)$$

where ΔRA and ΔDec are the difference in the RA and Dec coordinates of Toro as measured from Durham and La Palma at a given time. The baseline between Durham and La Palma can be approximated by the Haversine formula, which returns the distance between two points along a great circle on a sphere. Hence, we take the baseline to be approximately given by rearranging

$$\sin\left(\frac{B}{2R_{\oplus}}\right) \approx \sqrt{\sin^2\left(\frac{\Delta\varphi}{2}\right) + \cos\varphi_1 \cos\varphi_2 \sin^2\left(\frac{\Delta\lambda}{2}\right)}, \quad (5)$$

where R_{\oplus} is the radius of Earth, φ_1 and φ_2 are the latitudes of Durham and La Palma respectively, and $\Delta\varphi/\Delta\lambda$ are the differences in latitude/longitude between the two observatories. Using this formulation, along with the latitude and longitude positions for Durham and La Palma given in Table II and an Earth radius of approximately 6371 km, we calculate a baseline of $B \approx 3170$ km.

We calculate the parallax distance for many separate combinations of observations. Since these measurements are independent, we report their mean and standard deviation as the parallax distance and it's 1σ uncertainty. This uncertainty therefore encapsulates both the random uncertainties in the positional measurements, as well as random timing errors due to the fact that the combinations of observations used were not exactly simultaneous.

E. Photometric Measurements and Physical Characteristics

Asteroids have several key physical characteristics that are needed to understand their nature and quantify the risk they pose, namely their size, mass, and rotational period. To determine an asteroid's diameter, we first need to collect an observation of the asteroid in the V-band to measure it's V-band apparent magnitude, V . We first divide the observation by a flat-field image, taken by imaging a uniformly illuminated screen, to correct for pixel-to-pixel variations caused by dust grains and other debris on the surface of the telescope lens. From the number of background-subtracted counts collected from the object after flat-fielding, N , which we calculate via aperture photometry, it's V-band apparent magnitude is given by

$$V = -2.5 \log_{10}(N) + Z, \quad (6)$$

where Z is the zero-point of the image (i.e. the apparent magnitude of an object which gives 1 count per second on the CCD), which we determine by fitting the derived magnitudes of stars in the image to their catalogued magnitudes. From Poisson statistics, the uncertainty on the number of counts is given by \sqrt{N} , and hence a corresponding magnitude uncertainty can be determined by simple error propagation via the method outlined in appendix C. We then calculate the reduced magnitude, $H(\alpha)$, to remove the influence of distance on the V-band magnitude, leaving it to depend solely on the phase angle, α . The reduced magnitude is calculated via

$$H(\alpha) = V - 5 \log(r\Delta), \quad (7)$$

where r and Δ are the distances of the asteroid from the Sun and Earth respectively, both of which are calculated using

TABLE III. The three sets of observations used to produce light-curves, and hence determine the rotational period, for the asteroid Dembowska. Information regarding the date and duration of observations is included, as well as the filter used and exposure time of individual observations.

Observation Set	Date	Duration	Filter	Exposure Time
1	11/02/2024	~6.5 hrs	V	30 s
2	18/02/2024	~2.3 hrs	V	30 s
3	23/02/2024	~8.5 hrs	V	60 s

the methodology outlined in section II C. From this, we calculate the NEA's absolute magnitude, H , defined as the apparent magnitude when the NEA is both fully illuminated and at a distance of 1AU from the Earth and Sun. The absolute magnitude is given by

$$H = H(\alpha) + 2.5 \log_{10}((1 - G)\phi_1(\alpha) + G\phi_2(\alpha)), \quad (8)$$

where G is the slope parameter, assumed to be equal to 0.15 for all NEAs in accordance with JPL data (Giorgini et al. 1996), and

$$\phi_i(\alpha) = \exp(-A_i(\tan(0.5\alpha))^{B_i}). \quad (9)$$

The value of the constants A_i and B_i are taken to be $A_1 = 3.33$, $A_2 = 1.87$, $B_1 = 0.63$, and $B_2 = 1.22$ (Dymock 2007). The diameter of the asteroid, D , can then be calculated via Eq. (10) by assuming a value for the geometric albedo, A , which we take from the JPL Horizons system and are given in Table I.

$$D = 10^{3.1236 - 0.5 \log_{10}(A) - 0.2H} \quad (10)$$

We then estimate the mass of each NEA by assuming a uniform density, ρ , from the spectral type of the asteroid, as outlined in Table I. The mass can hence be calculated via

$$M = \frac{1}{6} \pi D^3 \rho. \quad (11)$$

An estimation of the mass of each NEA is of paramount importance as it allows their threat to be quantified on the Torino scale via a calculation of their impact energy, the process for which will be outlined in section II F.

The final physical characteristic we determine in this work is the rotational period. To determine the rotational period, long sequences of photometric observations are required in order to produce light-curves, which display the variation in the apparent magnitude of an asteroid as a function of time. With several separate light-curves, the rotational period of the asteroid can be estimated via phase dispersion minimisation (Stellingwerf 1978), which is a data analysis technique defined as the minimization of the dispersion (the difference between separate light-curves divided by their uncertainties) at different phases – the phase at which this is the minimum gives the best-fit rotational period.

It was not possible to determine the rotational periods of the four NEAs investigated in this work, mainly due to their relatively long rotation periods given in the available literature, combined with limited telescope time. Instead, we present a determination of the rotational period of the main-belt asteroid Dembowska to illustrate how this process could be carried out for NEAs without such tight time constraints. Table III shows the three sets of observations used to produce light curves in this work. A

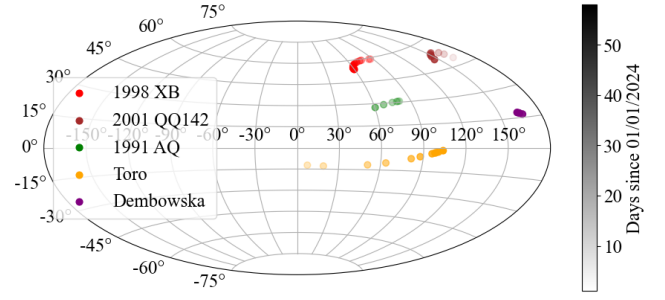


FIG. 5. The measured angular positions of the five asteroids studied in this work, plotted on a 2D projection of the sky. The opacity of each point represents the date on which the observation was taken, as shown by the colour bar on the right. The error bars are too small to be seen.

longer exposure time was used for observation set 3 due to a full moon in close proximity to the target. For each observation, we measure the background-subtracted counts on the CCD from Dembowska relative to two calibration stars, which mitigates unwanted variations due to variable weather conditions. The number of counts can then be converted into an apparent magnitude via Eq. (6). We then calculate the variation in the apparent magnitude from its median value as a function of time for each night to produce three light curves. We then proceed to carry out the phase dispersion minimisation process on these three light curves to determine the synodic rotation period of Dembowska.

We estimate the uncertainty on the rotation period using the grouped jackknifing technique (Shao and Wu 1989), where the phase dispersion minimisation process is carried out repeatedly, with one light curve removed from the set at a time, with the mean and standard deviation of the resulting values taken as the best-fit value and 1σ uncertainty on the rotation period. This technique was adopted over traditional jackknifing as it is significantly less computationally expensive for large datasets, but still captures the bias that each light curve imposes on the rotation period.

F. Impact Energies and Torino Scale Rankings

To quantify the risk posed by NEAs on the Torino Scale, an estimation of their impact energy is required. The impact energy is defined as the kinetic energy that an NEA would have at the point of collision should an impact with Earth occur. As such, the impact energy, E , is given by

$$E = \frac{1}{2} M v_{rel}^2, \quad (12)$$

where M is the mass of the NEA and v_{rel} is its velocity relative to Earth at the point of impact. The relative velocity can be discerned from the vis-viva equation, which gives the velocity of an object in an elliptical orbit, v . In the context of bodies orbiting the Sun, the vis-viva equation is given by

$$v = \sqrt{GM_{\odot} \left(\frac{2}{r} - \frac{1}{a} \right)}, \quad (13)$$

where G is Newton's Gravitational Constant ($G = 6.674 \times 10^{-11} \text{ Nm}^2 \text{ kg}^{-2}$), M_{\odot} is the solar mass ($M_{\odot} = 1.99 \times 10^{30} \text{ kg}$), r is the distance of the orbiting body from the centre of mass of the body-Sun system (which is approximately equal to the distance of the orbiting body from the Sun), and a is the semi-major axis of the orbiting body. Therefore, since

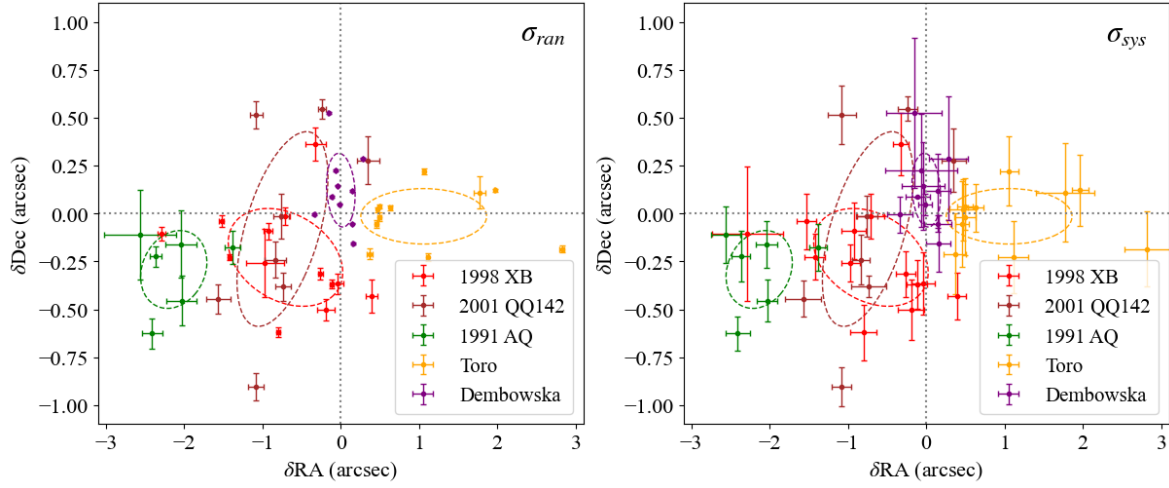


FIG. 6. The offsets of our positional measurements from the corresponding predictions on the JPL Horizons system (only including observations taken from Durham). On the left, error bars are included to represent only the random contribution to the positional uncertainty from the effect of seeing, and on the right, error bars are included to represent only the systematic contribution to the positional uncertainty arising from the star catalogue calibration. Dashed ellipses are included on both plots to represent the 1σ offsets from JPL, which are colour coded accordingly. It is clear that, for most of the asteroids studied, the systematic calibration uncertainty is dominant.

TABLE IV. The mean offsets of our positional measurements from those predicted by JPL for each asteroid, as shown graphically in Fig. IV.

Asteroid	δRA	δDec
1998 XB	$-0.70'' \pm 0.70''$	$-0.22'' \pm 0.25''$
2001 QQ142	$-0.75'' \pm 0.54''$	$-0.08'' \pm 0.48''$
1991 AQ	$-2.13'' \pm 0.39''$	$-0.29'' \pm 0.19''$
Toro	$1.06'' \pm 0.77''$	$-0.01'' \pm 0.14''$
Dembowska	$-0.0006'' \pm 0.1736''$	$0.12'' \pm 0.18''$

the heliocentric orbit of Earth is roughly circular, the orbital velocity of Earth can be found by inputting $r = a_{\oplus}$ and $a = a_{\oplus}$ into Eq. (13). The orbital velocity of each NEA can be determined by substituting $r = a_{\oplus}$ and $a = a_{NEA}$ into Eq. (13) since, at the theoretical point of impact, the distance of the NEA from the Sun would be the same as Earth's. Assuming that the NEA is moving in the same direction as Earth at the point of impact, the magnitude of the velocity of the NEA relative to Earth can be given by

$$v_{rel} = |v_{asteroid} - v_{\oplus}|. \quad (14)$$

This assumption is roughly valid since most asteroids, like Earth, are in counter-clockwise heliocentric orbits due to the counter-clockwise rotation of the accretion disk from which they all formed.

III. Results and Discussion

A. Astrometric Measurements

We first present the measured angular positions of each of the asteroids studied in this report on a 2D projection of the sky in Fig. 5. This graphical representation helps the reader to visualise the relative proper motion of each of the asteroids, as well as their dynamical evolution across the sky. It can be seen from Fig. 5 that the proper motion of the four NEAs, particularly Toro, was significant throughout the duration of the project. When this is combined with the relative faintness of many NEAs, necessitating the need for long exposures to achieve a sufficient SNR, it makes imaging NEAs challenging. Toro was also positioned at a very low declination for most observations, meaning it was close to the horizon. This not only adds to the challenge of imaging the object, but it also increases the effect of

seeing due to the additional atmosphere the telescope is looking through. The sole main-belt asteroid we investigate, Dembowska, can be seen to have a much lower proper motion as expected.

The mean offsets of our positional measurements from those predicted by the JPL Horizons system are shown both graphically in Fig. 6, and numerically in Table IV. It can be seen from the mean offset ellipses in Fig. 6 that only the positional measurements of Dembowska agree with the JPL predictions within 1σ , with an offset of less than $0.2''$ across both dimensions. On the other hand, the four NEAs have offsets of up to $3''$, corresponding to several pixels on the CCD. The $> 1\sigma$ offsets for the four NEAs could be attributed to their relatively large proper motions causing smearing across the CCD during long exposures, making it more difficult to accurately locate the centroid position of their 2D light profiles. Additionally, one should note the seemingly random ellipse positions and sizes in Fig 6 - there does not appear to be a clear systematic offset across all asteroids. However, upon closer inspection, it can be seen that the offsets are positively correlated with the direction of proper motion for each asteroid seen in Fig. 5 (e.g. Toro moves in the positive RA direction, and has a positive RA offset). This implies the presence of a timing error in our positional measurements, potentially caused by the time reported for each observation being the start of the exposure rather than the mid-point. This error would therefore be amplified for both long exposures and large proper motions, leading to the discrepancies seen for each NEA.

Fig. 6 also shows the relative sizes of the random and systematic contributions to the positional uncertainties. It is clear that for Dembowska, Toro, and 1998 XB, the systematic contribution to the uncertainty is dominant, whereas for 2001 QQ142 and 1991 AQ, the two contributions are more similar. Since the random contribution to the uncertainty is inversely proportional to the signal-to-noise ratio by Eq. (1), we expect that asteroids with a larger apparent magnitude will have a smaller random contribution to their positional uncertainty. This is exactly what is seen for Dembowska, Toro, and 1998 XB, whereas 2001 QQ142 and 1991 AQ were much fainter for the duration of observations, leading to a larger random

TABLE V. The six Keplerian orbital elements, along with their associated uncertainties (determined via jackknifing), and their corresponding epoch of osculation for each of the asteroids investigated in this work. Values for the perihelion and aphelion distances are also quoted with their uncertainties. Additional information regarding the number of observations used and the length of the observation arc are also given in the final two rows.

Parameter	1998 XB	2001 QQ142	1991 AQ	Toro	Dembowska
a [AU]	0.907894 ± 0.000004	1.42031 ± 0.00002	2.217 ± 0.006	1.36771 ± 0.00007	2.92391 ± 0.00001
e	0.35084 ± 0.00001	0.310072 ± 0.000009	0.777 ± 0.001	1.42031 ± 0.00002	0.08892 ± 0.00002
i [°]	13.5874 ± 0.0007	9.3369 ± 0.0002	3.120 ± 0.004	9.3834 ± 0.0004	8.25100 ± 0.00007
Ω [°]	75.6659 ± 0.0007	83.1497 ± 0.0009	339.43 ± 0.02	274.2401 ± 0.0008	32.1865 ± 0.0004
ω [°]	202.71497 ± 0.00008	337.9496 ± 0.0007	243.17 ± 0.07	127.229 ± 0.002	344.60 ± 0.01
M [°]	250.1517 ± 0.0006	49.9980 ± 0.0009	341.47 ± 0.09	52.737 ± 0.005	134.08 ± 0.01
q [AU]	0.58936 ± 0.00001	0.979912 ± 0.000002	0.494 ± 0.001	0.771175 ± 0.000005	2.66393 ± 0.00008
Q [AU]	1.226422 ± 0.000008	1.86071 ± 0.00004	3.94 ± 0.01	1.9642 ± 0.0001	3.18390 ± 0.00006
Epoch of Osculation	25/02/2024	18/02/2024	30/01/2024	27/02/2024	27/02/2024
# Obs.	12	12	6	10	5 (2024), 5 (2018)
Length of Obs. Arc	39 days	43 days	17 days	43 days	16 days (2024), 43 days (2018)

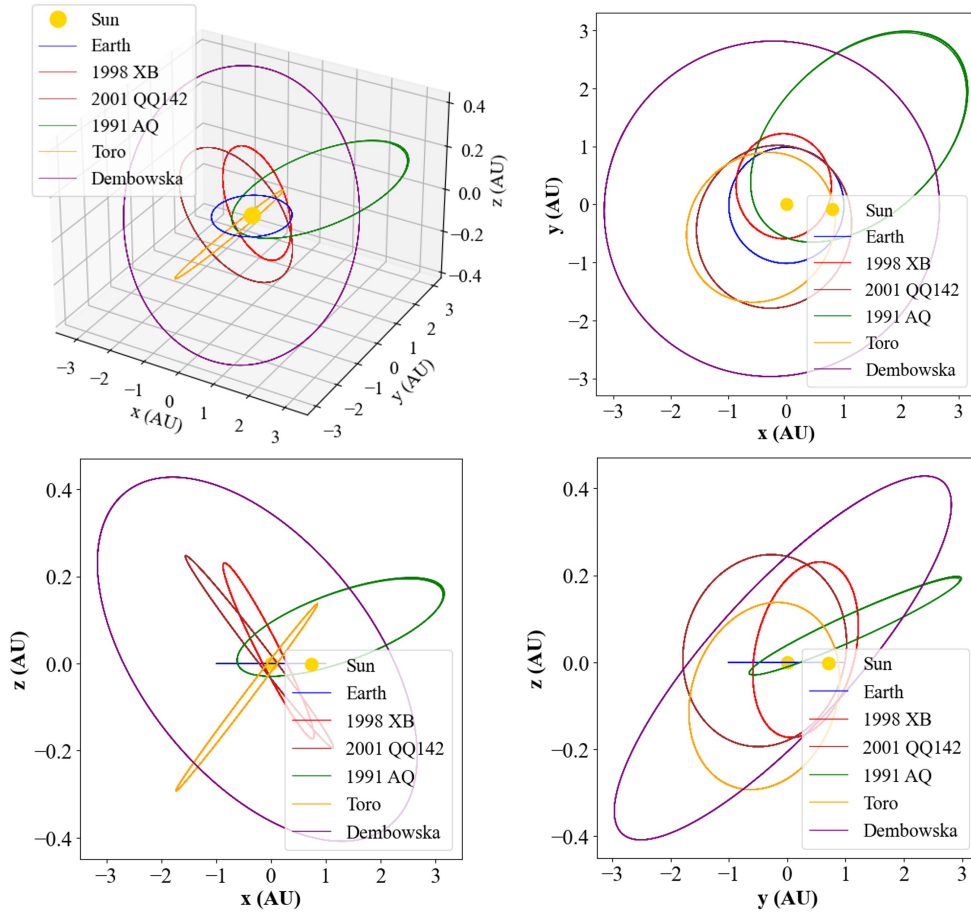


FIG. 7. The orbits of each of the asteroids investigated in this work, visualised on a 3D plot (top left), and in the x-y plane (top right), x-z plane (bottom left), and y-z plane (bottom right). The orbits for a number of virtual asteroids are plotted for each target. The orbit of the Earth is also included in blue, and the (essentially constant) position of the Sun is marked in yellow. Legends are included on each plot to inform the reader which colour corresponds to which asteroid. One can see that each NEA has an orbit which intersects that of Earth, and the classifications of each asteroid as either Apollo/Aten/main-belt can be inferred from the shape of their orbits in the x-y plane.

contribution to their positional uncertainty. The systematic contribution arises from the star catalogue calibration, which is dependent on the number of stars detected in the image whose position can be accurately determined - a denser star field in the image, along with no saturation and good seeing conditions, will allow for a more accurate and precise positional calibration. The number of stars detected in each observation is given in Appendix A, from which one can note that the number of stars detected in the observations for each individual asteroid are a similar

order of magnitude to each other, which leads to the similar systematic uncertainties seen for each asteroid in Fig. 6.

B. Orbits

As outlined previously, the astrometric measurements and uncertainties can be passed into *find_orb*, which returns the best-fit orbital parameters, with their corresponding uncertainties found via jackknifing. The six Keplerian orbital elements for each asteroid, along with the perihelion and aphelion distances, are quoted in Table V along with

their 1σ uncertainties. These orbital elements, along with their epoch of osculation, can be converted into coordinates in a cartesian heliocentric coordinate system at any future epoch, allowing the orbits of each asteroid to be visualised in both two and three dimensions, as shown in Fig. 7.

We first focus on the NEA Toro, for which the parameters given in Table V satisfy both $a > 1.0$ AU and $q < 1.017$ AU, confirming Toro's status as an Apollo class NEA. This can also be confirmed by inspecting the shape of Toro's orbit relative to that of Earth in the x-y plane in Fig. 7 - it is clear that Toro does indeed intersect Earth's orbit, with a semi major axis which is greater than that of Earth. This validates our treatment of Toro as an NEA, and thus prompts us to quantify the risk posed by Toro on the Torino scale. Similarly, the orbital parameters returned for 2001 QQ142 and 1991 AQ also satisfy $a > 1.0$ AU and $q < 1.017$ AU, confirming their status as Apollo class NEAs.

For the asteroid 1998 XB, we find that the orbital parameters in Table V instead satisfy $a < 1.0$ AU and $Q < 0.983$ AU, as would be expected for an Aten class NEA. Similar to above, the classification of 1998 XB can also be inferred from the orbit visualisations given in Fig. 7, which clearly show the orbit of 1998 XB intersecting that of Earth, with a semi major axis that is smaller than Earth's. Whilst this is a different classification of NEA, it still possesses an Earth-crossing orbit, and hence the risk it poses should still be investigated.

For the asteroid Dembowska, we find a perihelion distance of $q = 2.66393 \pm 0.00008$ AU, showing that Dembowska's orbit does not intersect with that of Earth, as would be expected for a main-belt asteroid. This confirms that Dembowska is not an NEA and hence poses no threat to civilisation on Earth, rendering it meaningless to calculate impact probabilities/Torino scale rankings for this asteroid.

Since the uncertainties on the orbital parameters are found via jackknifing, they are resistant to outlying/erroneous astrometric measurements as *find_orb* automatically rejects measurements which produce large residuals during the fitting process. If this was not the case, then outlying astrometric measurements would have the potential to skew the results and produce uncertainties that are too large. Furthermore, it is noticeable that the uncertainties on the orbital parameters for each asteroid vary significantly. For example, the fractional uncertainties for 1991 AQ are several orders of magnitude larger than those for 1998 XB and 2001 QQ142. It is also clear from the information regarding the number of observations and the length of the observation arcs given in Table V that larger orbital uncertainties are correlated with a lower number of observations and a shorter observation arc, as would be expected intuitively. Therefore, as the orbital uncertainties are resistant to outliers and scale as expected with the number of observations included in the analysis, we conclude that they are reliable and robust.

Using the derived orbital parameters and their uncertainties, we proceed to determine each NEA's distance from Earth (and the associated uncertainty) via the Monte Carlo approach outlined in section II C. Fig. 8 shows how the distance uncertainty scales with time for each NEA. Whilst there is a significant aliasing effect, it is clear that the general trend for all asteroids is a linear increase with time. Since these distances are ultimately derived from the orbital parameters, we intuitively expect that larger orbital uncertainties will lead to larger distance

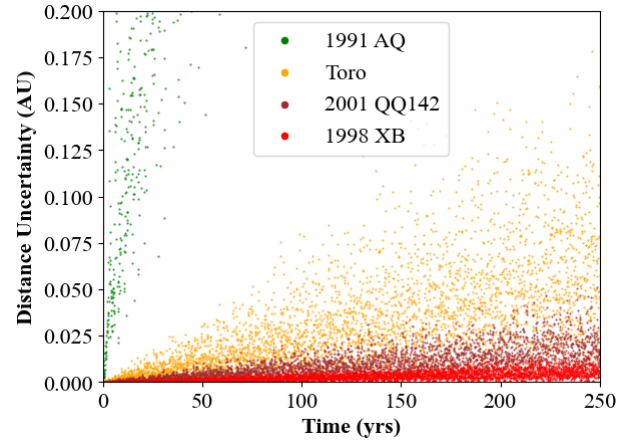


FIG. 8. The uncertainty on the Earth-asteroid distance for each NEA as a function of time. It can be seen that the distance uncertainty scales most rapidly for 1991 AQ, which has the largest orbital uncertainties.

uncertainties. This is exactly what is seen in Fig 8, where the distance uncertainties for 1991 AQ, which has the largest orbital uncertainties in Table V, are the most significant and scale most rapidly with time. The fact that the distance uncertainty scales as expected, and shows the intuitively correct dependence on the orbital uncertainties, provides confidence that the derived uncertainties, and thus the associated methodology, are valid.

Fig. 9 shows the distance from Earth of the asteroid Toro for the next decade (starting from the date of the final observation), along with the normalised residuals between the distances predicted in this work and those given by JPL (i.e. the difference between the two divided by the uncertainties). The JPL distances are included as a separate independent prediction of the Earth-asteroid distance for comparison purposes. One can see a clear multi-modal oscillation arising from the different orbital dynamics of Earth and Toro, as would be expected. Whilst the $< 3\sigma$ difference between the predicted and JPL distances for the majority of epochs is encouraging, the primarily notable peaks in the normalised residuals at ~ 1600 and ~ 1900 days, corresponding to the two points of closest approach in the next decade, indicate a discrepancy between the two methodologies. One key discrepancy is that, in this work, future gravitational interactions are not taken into account and hence the orbital parameters for each NEA are assumed to be constant in time. In reality, gravitational encounters with other solar system bodies have the potential to perturb orbits. It may intuitively be expected that, if this were the cause of the peaks in the normalised residuals seen in Fig. 9, then we would expect the orbit to be permanently perturbed and hence the normalised residuals to remain high, rather than returning to low values after the point of closest approach. However, as is evidenced by the larger uncertainties towards the minima in the cutout plot in Fig. 9, the Earth-asteroid distance becomes more sensitive to small perturbations in the orbital parameters at the points of closest approach. This means that a small difference between the orbital parameters determined in this work and those given by JPL would lead to amplified differences between the two distance predictions at these points. This indicates a need to include the effects of gravitational perturbations in future NEA analyses to provide more accurate results.

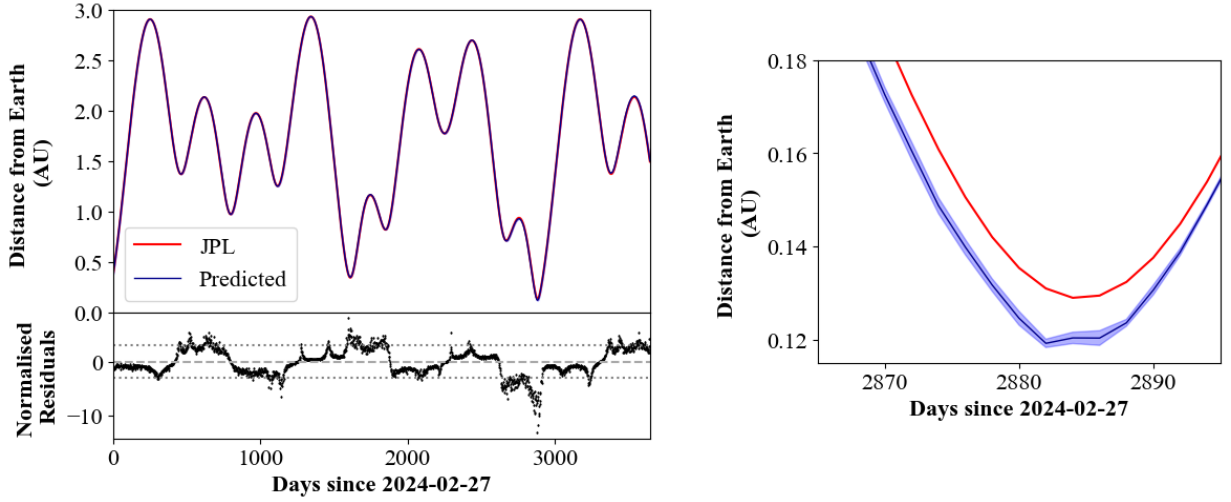


FIG. 9. Left: The distance from Earth of the asteroid Toro over the next decade. The distance predicted by this work are shown in blue, and the distances given by JPL are shown in red for comparison purposes. The x-axis shows the number of days since the date of our final observation of Toro. The bottom plot shows the difference between the distances predicted by this work and those given by JPL, divided by their uncertainty (i.e. normalised residuals). One can see that the discrepancy is $< 3\sigma$ for the majority of the timeframe, but has peaks of up to $> 10\sigma$ at the points of closest approach. Right: A cutout of the plot on the left around the point of closest approach in the next decade to make it easier for the reader to discern the difference between the predicted and JPL values. The 1σ uncertainty range for the distances predicted by this work is shown in a more transparent blue. One can see that the predicted distances do not agree with those given by JPL within 1σ , and the difference between the two becomes more pronounced at the point of closest approach.

C. Parallax Measurement

We proceed to present the results for a set of simultaneous observations taken from observatories at both Durham and La Palma on the night of 18/02/2024, starting at 20:54:22 UTC, for the asteroid Toro. A measurement of Toro's distance from Earth via parallax is an independent distance measurement which can be compared to the predicted distances to further investigate their accuracy. 30s exposures were set running on both telescopes for a period of up to 20 minutes, and an astrometric analysis was performed on the six observations taken at La Palma with both the best seeing conditions and the most visible catalogue stars, along with the six corresponding observations from Durham which were closest in time to those chosen from La Palma. Fig. 10 shows the measured right ascension and declination coordinates for the 12 chosen observations, colour coded by the reported time that the observation was taken, along with dashed black lines to represent the tracks of Toro across the sky as viewed from each observatory.

When the formulation outlined in section II D is applied to each of the six combinations of measurements, and the mean and standard deviation of each of these independent measurements is taken, we obtain a result of $d = 0.40 \pm 0.01$ AU for the parallax distance. This assumes all six measurements were taken at the same time, which is a reasonable assumption considering there are only ~ 6 minutes between the first and last observation used, and Toro's distance from Earth is unlikely to change by much during this time. The predicted distance at the time of the parallax measurements, determined via the 10000 virtual asteroids initialised previously, is 0.29943 ± 0.00007 AU. One can see that the measured parallax distance is not in agreement with the predicted distance within its uncertainty range. Since, from Fig. 9, the percentage difference between the predicted and JPL distances is significantly less than the percentage difference between the predicted and parallax distances, we conclude that there

is likely to be an inaccuracy in our determination of the parallax distance. From Fig. 10, one should note that the two tracks, whilst parallel, are inclined, which induces an increased risk of random timing errors. However, since the reported time between pairs of measurements was only a few seconds, and the effect of random timing errors is encapsulated within the parallax distance uncertainty, we conclude that this would not be the cause of the $>> 1\sigma$ offset found for the parallax distance. There could however be an unknown systematic offset in the times reported for observations at either the Durham or La Palma observatories which, while unlikely to be significant, could contribute to the difference between the measured and expected distances. One should also note that, as outlined in the methodology, we take the baseline to be given by the Haversine formula, which returns the distance along the curved edge of a sphere. In reality, for the geometry of Eq. (3) to be correct, the baseline should be taken as the chord between the two observatory locations. This would lead to an overestimate of the true baseline, and hence an overestimate of the parallax distance. However, the effect of this on the final result would not be significant since the radius of Earth is much larger than the arc length between the two observatory locations. Similarly, the Earth's non-spherical nature and ellipticity would lead to small inaccuracies, but these would not be sufficient to explain the $\sim 25\%$ discrepancy. When investigating the JPL offsets for each set of astrometric measurements, we find a mean offset of $\delta_{\text{RA}} = 0.63 \pm 0.03$ and $\delta_{\text{Dec}} = 0.15 \pm 0.02$ for observations taken from Durham, and $\delta_{\text{RA}} = 0.56 \pm 0.22$ and $\delta_{\text{Dec}} = 0.22 \pm 0.10$ for observations taken from La Palma. Whilst there is a small difference in the offsets for each observatory, it is of the order of a tenth of an arcsecond, which is again insufficient to explain the disagreement between the expected and parallax distances.

We have discussed several factors which in isolation are insufficient to explain the discrepancy in the parallax distance, but when combined could significantly perturb the parallax distance from its true value.

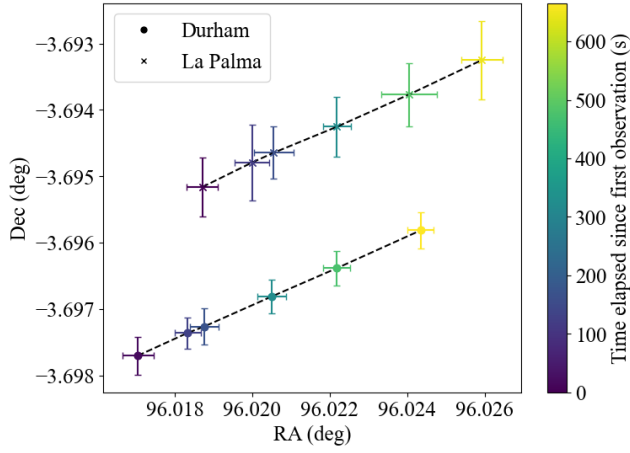


FIG. 10. The measured angular positions for six (almost) simultaneous sets of observations taken from observatories at Durham and La Palma. Error bars are included to represent 10σ uncertainties to make them more visible to the reader. Each data point is colour coded by the time elapsed since the first observation was taken. Two dashed black lines are included to represent the tracks of Toro across the sky. From this visualisation, one can clearly see the six combinations of measurements used to calculate parallax distances via the colour mapping, as well as the parallel, non-horizontal nature of Toro’s proper motion.

D. Impact Probabilities, Physical Characteristics, and Torino Scale Rankings

We present the impact probabilities, physical characteristics, and Torino Scale rankings for each NEA. When choosing the time range over which we find the closest approach for each NEA, we consider the rate at which the distance uncertainties scale in Fig. 8 such that we obtain meaningful results - we consider the next five years for 1991 AQ, the next decade for Toro, and the next century for 1998 XB and 2001 QQ142. Fig. 11 shows cumulative histograms for the closest approach distance and date within the next decade for the asteroid Toro, along with the fitted CDFs in red, from which we obtain a close approach distance of 0.119 ± 0.003 AU and a closest approach date of 2463251.4 ± 0.3 Julian Days, corresponding to a UTC date/time (in format YYYY-MM-DDThh:mm:ss) of $2032-01-19T21:36:00 \pm 7$ h. From the closest approach distance CDF, we determine the probability of Earth impact as the value of the CDF at an Earth-asteroid distance of one Earth radius. Table VI shows the results of this process for each NEA. The corresponding physical characteristics and Torino Scale rankings are shown in Table VII.

One can see from Table VII that the close approach events for 1998 XB, 2001 QQ142, and Toro have all been categorized as a 0 on the Torino scale, indicating that these events have no likely consequences and thus do not need close, continued monitoring. This is due to the extremely low impact probabilities for all of these events, owing to the small uncertainties on the orbital parameters, and thus the close approach distance. On the contrary, the close approach event for 1991 AQ has been assigned a provisional Torino scale ranking of 1, indicating that this is an event which requires careful monitoring. This ranking owes mostly to the relatively large impact probability for the 1991 AQ close approach event given in Table VI, which arises from the large orbital uncertainties for this NEA. Therefore, it is likely that with additional observations included in the analysis, this impact probability would decrease, thus

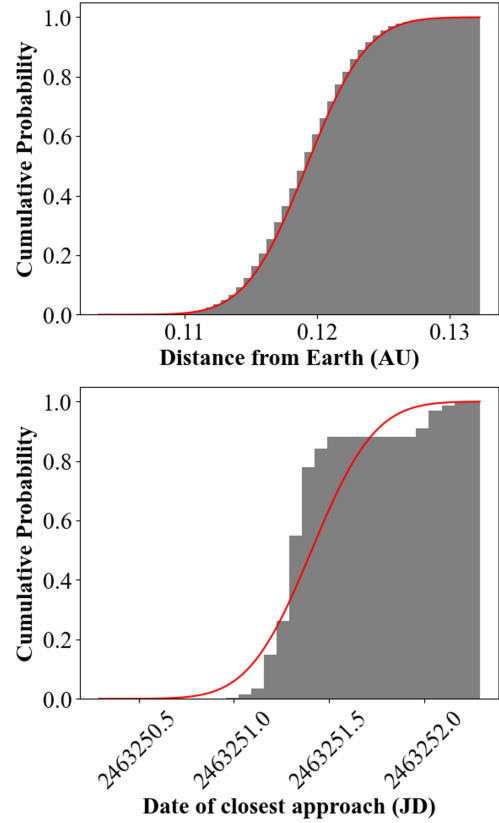


FIG. 11. Cumulative histograms (grey) of the closest approach distance and date (in Julian Days) of 10000 virtual asteroids in the next decade for the asteroid Toro. CDFs constructed via the mean and standard deviation of the virtual asteroid’s distances/dates of closest approach are shown in red.

downgrading the Torino scale ranking to 0. Additional observations would also allow for more tightly constrained orbits, allowing impact events further into the future to be investigated without the associated uncertainties becoming too large. One should note that the impact velocities and energies reported in Table VII are lower bounds on the true values due to the assumption that the Earth and asteroid are travelling in the same direction at the point of impact - the true values would be larger if the Earth and asteroid were instead travelling in non-parallel directions.

E. Rotational Period

Finally, we present the results of the phase dispersion minimisation process used to determine the synodic rotation period of Dembowska. Fig. 12 shows the three light curves produced from the three sets of observations given in Table III, one of which clearly does not extend the duration of one full rotational period. Fig. 13 shows the dispersion, which was calculated from a period of 0.16d to a period of 0.24d in 1000 bins, as a function of period, from which one can see that the dispersion minimum is successfully being located. We determine the period at which the dispersion is minimum as $P = 4.68 \pm 0.15$ hours, with the uncertainty determined via grouped jackknifing, as outlined previously. We note that this value is in agreement within 1σ with the rotation periods for Dembowska given by both Torppa et al. (Torppa et al. 2003) and the JPL database (Giorgini et al. 1996), providing confidence that the adopted methodology is valid. With only three light curves included in the analysis, one of which does not extend over a full period, the uncertainty on the rotational period is relatively large.

TABLE VI. The closest approach distances, dates, and impact probabilities for the four NEAs investigated in this work. An impact probability of $< 10^{-100}$ has been reported as 0. The 'timescale considered' column informs the reader of the range of time from which the closest approach was determined. The probability of each asteroid passing within 0.05 AU of Earth is also included, as this is the condition required for an NEA to be considered 'potentially hazardous' by NASA's CNEOS.

Asteroid	Timescale considered	Closest approach distance [AU]	Closest approach date [JD]	Impact Probability	<0.05 AU Probability
1998 XB	100 years	0.113749 ± 0.000006	2469394.52 ± 0.01	0	0
2001 QQ142	100 years	0.014 ± 0.002	2468327.6 ± 0.5	$\sim 10^{-19}$	1.0
1991 AQ	5 years	0.34 ± 0.09	2461650 ± 4	$\sim 10^{-4}$	$\sim 10^{-3}$
Toro	10 years	0.119 ± 0.004	2463251.4 ± 0.3	0	$\sim 10^{-82}$

TABLE VII. The estimated physical characteristics, impact energies, and Torino scale rankings for the four NEAs investigated in this work. A diameter has been taken from the JPL Horizons system for 1991 AQ due to a lack of V-band measurements for this object.

Asteroid	Diameter [km]	Mass [kg]	Impact Velocity [m/s]	Impact Energy [Mton]	Torino Scale Ranking
1998 XB	0.72 ± 0.03	$(5.3 \pm 0.7) \times 10^{11}$	1549.3 ± 0.1	150 ± 20	0
2001 QQ142	0.61 ± 0.03	$(3.1 \pm 0.4) \times 10^{11}$	4144.6 ± 0.1	640 ± 90	0
1991 AQ	1.1 (Giorgini et al. 1996)	1.9×10^{12}	7280 ± 20	11950 ± 50	1
Toro	3.49 ± 0.04	$(6.0 \pm 0.2) \times 10^{13}$	3760.9 ± 0.5	101500 ± 3000	0

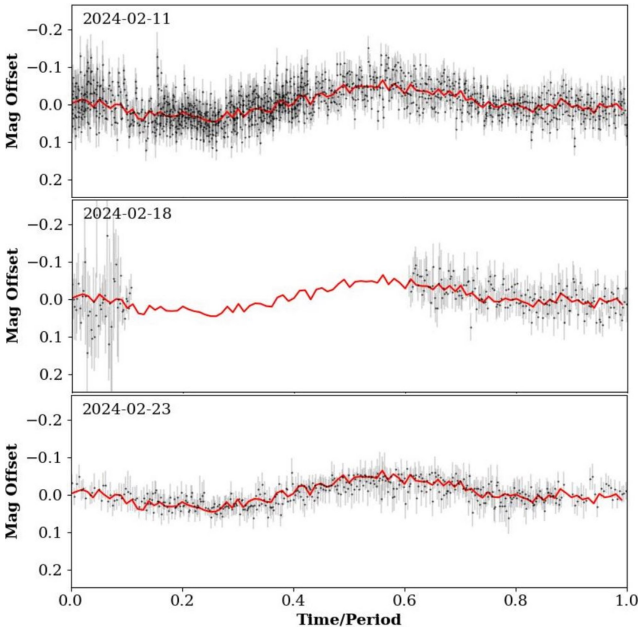


FIG. 12. The three light curves produced for Dembowska. The y-axis is the magnitude variation from the median value, and the x-axis is the phase of rotation. Data points are shown in black, with their error bars in grey. All data points have been folded back into one rotational period. The best-fit model is shown in red.

With additional project time, further sets of observations could be taken in order to produce additional light curves to be included in the analysis, which would increase both the accuracy and precision of the final result. This additional time would also allow for a similar investigation of NEAs with a longer rotation period.

In future projects, with a larger number of light curves for a given asteroid, and thus a tighter constraint on the rotational period, light curve inversion (Torppa et al. 2003) could be performed to produce a 3D model of the asteroid, from which its physical characteristics can be inferred more accurately.

F. Limitations and Potential Improvements

There are several limitations to this work which should be discussed, the most significant of which is the overlook of gravitational effects. Whilst significant gravitational

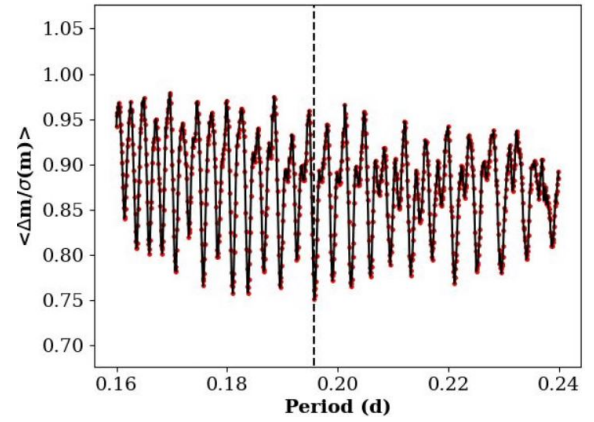


FIG. 13. The dispersion as a function of rotational period (in days) for the asteroid Dembowska. The dispersion has been calculated for $\pm 10\%$ around a period of 0.20 days in 1000 bins. A vertical dashed black line is included to indicate the period at which the dispersion is minimised.

encounters are rare due to the vastness of space, they have the potential to perturb orbits, thus affecting orbital parameters, impact probabilities and energies, and therefore Torino scale rankings. We have also ignored the possibility of collisions between asteroids and other bodies which, while again rare, could significantly alter the results. To take gravitational effects into account, dynamical modelling of all solar system bodies would be required in order to locate any close approaches between NEAs and other solar system bodies, and determine how the orbital parameters are perturbed as a result. This would be particularly computationally expensive and would induce additional uncertainties due to the extra orbital modelling that would be required.

Additionally, there are further non-gravitational effects, such as the Yarkovsky orbital drift (Rozitis 2014), which have the potential to significantly alter orbits over time, and hence should be taken into account to provide a more accurate orbital determination. Modelling of the Yarkovsky effect is however highly complex and requires pre-determined knowledge of the asteroid's topology and physical characteristics (Rozitis 2014).

Another major limitation arose from the relative faintness of many of the NEAs, necessitating long exposures. When combined with their large proper motion, this led to

significant smearing across the CCD, making it extremely difficult to determine the centroid coordinates of the asteroid via the 2D Gaussian fitting method adopted in this work. Techniques that use a large number of short exposures, such as synthetic tracking as proposed by (Shao et al. 2014), can be used to remove this CCD smearing and provide increased sensitivity for locating small, faint, and fast-moving NEAs. Telescopes with a larger aperture size could also be used in future studies to make it easier to resolve fainter objects. All NEAs studied in this report became gradually fainter throughout the duration of the project as they moved further away from Earth which, particularly for 1991 AQ and 2001 QQ142, limited the number of observations that could be taken. A greater resolving power would allow for longer observation arcs as each NEA would be resolvable for a longer period of time, thus reducing the orbital uncertainties and providing revised Torino scale rankings.

IV. Conclusions

In this work, we have quantified the risk posed by several NEAs on the Torino Scale via a series of observations taken from observatories located in both Durham, UK and La Palma, Spain. We determined constraints on the orbital parameters for 1998 XB, 2001 QQ142, 1991 AQ, Toro, and Dembowska via astrometric measurements performed on these observations. The random and systematic contributions to the astrometric uncertainties were discussed, from which it was concluded that the systematic calibration contribution was dominant. From the derived constraints on the orbital parameters, impact probabilities were calculated for each NEA. V-band photometric measurements were then used to estimate each NEA's physical characteristics, from which their impact energies, and thus Torino scale rankings, could be determined. We assigned a Torino scale ranking of 0 to all NEAs except 1991 AQ, which was given a provisional rating of 1 for a close approach event in 2027. It was concluded that, whilst this rating indicates that 1991 AQ requires careful monitoring, it would likely be downgraded if additional observations were included in the analysis to reduce the orbital uncertainties.

We also carried out a parallax distance measurement for Toro, which was compared to the distance predicted by our orbital parameters in an attempt to validate our results. We determined a parallax distance of $d = 0.40 \pm 0.01$ AU, which was not in agreement with the predicted distance of 0.29943 ± 0.00007 AU within 1σ . It was concluded that this discrepancy was most likely due to an accumulation of several small inaccuracies, including potential unknown systematic timing errors, inaccurate assumptions in the methodology, and offsets in the astrometric measurements.

Finally, we noted that alternative methodologies which allow for fainter objects to be resolved on the CCD, such as synthetic tracking (Shao et al. 2014), could be adopted in future NEA studies in order to obtain longer observation arcs, and thus smaller orbital uncertainties. Additional dynamical modelling could also be carried out to include future gravitational perturbations on the NEA orbits.

Acknowledgments

The author would like to express deep gratitude to both Prof. Mark Swinbank and Prof. Alastair Edge for their

immense help and support throughout the duration of this project. The author would also like to thank the Durham Physics Department for allowing students the opportunity to use the telescopes on the roof of the Physics building to take our own observations.

References

- [1] Emel'yanenko, V.V. et al. (2013) 'Astronomical and physical aspects of the Chelyabinsk event (February 15, 2013)', *Solar System Research*, 47(4), pp. 240–254. doi:10.1134/s0038094613040114.
- [2] Chiarenza, A.A. et al. (2020) 'Asteroid impact, not volcanism, caused the end-cretaceous dinosaur extinction', *Proceedings of the National Academy of Sciences*, 117(29), pp. 17084–17093. doi:10.1073/pnas.2006087117.
- [3] Adams, R. B. et al. (2004) 'Survey of technologies relevant to defense from near Earth objects', NASA, NASA/TP-2004-213089.
- [4] Bancelin, D. et al. (2012) 'Asteroid (99942) Apophis: New predictions of Earth encounters for this potentially hazardous asteroid', *Astronomy & Astrophysics*, 544. doi:10.1051/0004-6361/201117981.
- [5] Birlan, M. et al. (2010) 'More than 160 near earth asteroids observed in the Eurnear Network', *Astronomy and Astrophysics*, 511. doi:10.1051/0004-6361/200912865.
- [6] Shin, Y. et al. (2015) 'Radiation effect for a CubeSat in slow transition from the Earth to the Moon', *Advances in Space Research*, 55(7), pp. 1792–1798. doi:10.1016/j.asr.2015.01.018.
- [7] Giorgini, J.D. et al. (1996) 'JPL's On-Line Solar System Data Service', *Bulletin of the American Astronomical Society*, 28(3), pp. 1158, 1996. ADS Bibcode: 1996DPS....28.2504G
- [8] Krasinsky, G. (2002) 'Hidden Mass in the Asteroid Belt', *Icarus*, 158(1), pp. 98–105. doi:10.1006/icar.2002.6837.
- [9] Kaiser, N. (2004) 'Pan-STARRS: A wide-field optical survey telescope array', *SPIE Proceedings*. doi:10.1117/12.552472.
- [10] Christensen, E. et al. (2012) 'The Catalina Sky Survey: Current and Future Work', *American Astronomical Society Division for Planetary Sciences Meeting Abstracts*, 44, pp. 210.13. ADS Bibcode: 2012DPS....4421013C.
- [11] Lam, A.L. et al. (2023) 'Determination of 1929 asteroid rotation periods from Wise Data', *The Planetary Science Journal*, 4(4), p. 61. doi:10.3847/psj/acc5e4.
- [12] Gray, B. (2022) Find.Orb Orbit Determination Software. ADS Bibcode: 2022ascl.soft02016G
- [13] Sakai, S. et al. (2019) 'The Galactic Center: An improved astrometric reference frame for stellar orbits around the supermassive black hole', *The Astrophysical Journal*, 873(1), p. 65. doi:10.3847/1538-4357/ab0361.
- [14] Dymock, R. (2007), 'The H and G magnitude system for asteroids', *Journal of the British Astronomical Association*, 117, pp. 342–343. ADS Bibcode: 2007JBAA..117..342D
- [15] Stellingwerf, R.F. (1978) 'Period determination using phase dispersion minimization', *The Astrophysical Journal*, 224, p. 953. doi:10.1086/156444.
- [16] Shao, J. and Wu, C.F. (1989) 'A general theory for jackknife variance estimation', *The Annals of Statistics*, 17(3). doi:10.1214/aos/1176347263.
- [17] Torppa, J. et al. (2003) 'Shapes and rotational properties of thirty asteroids from Photometric Data', *Icarus*, 164(2), pp. 346–383. doi:10.1016/s0019-1035(03)00146-5.
- [18] Rozitis, B. (2014), 'Modeling of the Yarkovsky and YORP effects', p. 454. ADS Bibcode: 2014acm.conf.454R
- [19] Shao, M. et al. (2014) 'Finding very small near-Earth asteroids using synthetic tracking', *The Astrophysical Journal*, 782(1), p. 1. doi:10.1088/0004-637x/782/1/1.

Scientific Summary for a General Audience

The early Solar system was extremely chaotic, with frequent collisions between bodies releasing large amounts of debris. Much of this debris has since coalesced into millions of small chunks of rock and ice flying through our Solar system at thousands of miles per hour, which we call asteroids. Most known asteroids have settled into stable orbits between Mars and Jupiter, but a small percentage have orbits which bring them into close proximity with Earth, and are aptly named Near Earth asteroids (NEAs), with new NEAs being discovered every day. The Torino scale was proposed in 1999 as an analogue to the Richter scale to categorize the threat posed by NEAs, encapsulating both the likelihood and consequences of a potential collision. Recent scares, such as the Chelyabinsk event in 2013, where an asteroid larger than a house entered Earth's atmosphere and exploded over the city of Chelyabinsk in Russia, have sparked further interest in the study and tracking of NEAs and show that, whilst space is vast, we are not immune to it's highly dynamical and dangerous nature.

In this work, we determine the orbits and impact probabilities of several NEAs and estimate their physical characteristics such that their threat can be quantified on the Torino scale.

Appendix A: Observation Logs and Example Measurements

Date + Time	Telescope	Filter	Exp. Time (s)	# Stars Detected	S/N	RA	$\sigma_{\text{sys, RA}}$ [arcsec]	FWHM (RA)	$\sigma_{\text{ran, RA}}$ [arcsec]	Dec	$\sigma_{\text{sys, Dec}}$ [arcsec]	FWHM (Dec)	$\sigma_{\text{ran, Dec}}$ [arcsec]
2024-01-17T18:22:38.685	Draco2	C	15	67	3.43E+01	05:48:34.827	0.168	5.3	0.066	59:03:11.11	0.116	3.77	0.047
2024-01-18T18:02:31.9696	East-16	C	30	169	4.18E+01	05:41:33.155	0.124	3.65	0.037	59:10:16.28	0.146	3.11	0.032
2024-01-24T19:53:33.991	Draco2	C	30	78	6.08E+00	05:03:16.013	0.121	3.45	0.241	59:10:39.39	0.098	2.56	0.179
2024-01-26T18:27:58.581	Far-East-20	C	60	40	3.57E+01	04:53:09.810	0.453	4.24	0.050	58:58:59.20	0.350	2.98	0.035
2024-01-30T20:18:47	East-16	C	60	411	7.60E+01	04:35:19.477	0.134	3.58	0.020	58:23:39.47	0.120	2.87	0.016
2024-02-03T22:19:10.414	Draco2	C	60	216	2.80E+01	04:21:47.415	0.153	3.64	0.055	57:39:57.51	0.147	2.86	0.043
2024-02-11T21:25:19.408	West-14	C	120	366	4.99E+01	04:05:41.745	0.170	3.27	0.028	56:11:00.88	0.145	3.02	0.026
2024-02-18T19:42:21	East-16	C	90	313	3.19E+01	03:59:51.904	0.126	2.24	0.030	55:02:17.78	0.12	2.3	0.031
2024-02-20T21:52:24	Draco2	C	90	189	3.43E+01	03:59:10.104	0.148	3.91	0.064	54:43:50.55	0.163	3.34	0.054
2024-02-21T18:57:32.421	Draco2	C	90	240	4.18E+01	03:59:00.928	0.126	2.26	0.025	54:36:30.88	0.127	2.22	0.024
2024-02-23T19:48:05.680	West-14	C	120	137	6.08E+00	03:58:52.228	0.169	4.65	0.112	54:20:04.85	0.159	2.41	0.058
2024-02-25T21:06:17.543	Pt5m	V	120	31	3.57E+01	03:59:02.259	0.046	4	0.133	54:04:37.70	0.087	4	0.133

FIG. 14. Observation log and astrometric measurements for 1998 XB.

Date + Time	Telescope	Filter	Exp. Time (s)	# Stars Detected	S/N	RA	$\sigma_{\text{sys, RA}}$ [arcsec]	FWHM (RA)	$\sigma_{\text{ran, RA}}$ [arcsec]	Dec	$\sigma_{\text{sys, Dec}}$ [arcsec]	FWHM (Dec)	$\sigma_{\text{ran, Dec}}$ [arcsec]
2024-01-06T20:01:44.899	Draco2	C	30	21	1.13E+01	10:55:58.384	0.158	3.91	0.147	48:52:06.41	0.165	3.34	0.126
2024-01-12T22:15:29.395	Draco2	C	60	27	2.72E+01	10:49:41.127	0.126	3.38	0.053	51:33:43.46	0.063	3.31	0.052
2024-01-17T18:33:03	Draco2	C	90	23	2.53E+01	10:42:10.003	0.181	4.79	0.080	52:57:15.42	0.154	4.16	0.070
2024-01-30T20:31:02.734	East-16	C	90	52	1.32E+01	10:16:22.713	0.108	4.32	0.139	54:07:22.38	0.129	2.96	0.095
2024-02-03T02:54:32.712	Pt5m	V	90	15	1.83E+01	10:09:43.340	0.062	1.76	0.041	53:55:22.71	0.033	1.97	0.046
2024-02-03T22:30:32.269	Draco2	C	90	33	1.44E+01	10:08:08.774	0.136	3.35	0.099	53:50:16.93	0.107	3.99	0.118
2024-02-07T19:48:31.026	Draco2	C	180	21	8.60E+00	10:00:49.753	0.230	3.13	0.155	53:19:18.00	0.096	1.55	0.077
2024-02-08T00:06:43.309	Pt5m	V	90	7	3.90E+00	10:00:29.990	0.097	5.00	0.545	53:17:58.61	0.062	4.00	0.436
2024-02-11T05:49:59.719	Pt5m	V	120	8	1.50E+01	09:55:05.489	0.076	3.91	0.110	52:45:27.59	0.029	1.96	0.055
2024-02-11T20:45:52.395	West-14	C	90	28	1.43E+01	09:54:00.239	0.221	3.40	0.101	52:34:12.42	0.056	2.42	0.072
2024-02-12T01:27:33.904	Pt5m	V	120	11	1.66E+01	09:53:40.308	0.187	1.49	0.038	52:32:03.14	0.032	3.57	0.092
2024-02-18T19:24:39.237	East-16	C	180	50	1.32E+01	09:44:44.222	0.124	3.19	0.103	50:51:06.62	0.101	2.18	0.070

FIG. 15. Observation log and astrometric measurements for 2001 QQ142.

Date + Time	Telescope	Filter	Exp. Time (s)	# Stars Detected	S/N	RA	$\sigma_{\text{sys, RA}}$ [arcsec]	FWHM (RA)	$\sigma_{\text{ran, RA}}$ [arcsec]	Dec	$\sigma_{\text{sys, Dec}}$ [arcsec]	FWHM (Dec)	$\sigma_{\text{ran, Dec}}$ [arcsec]
2024-01-13T19:51:33.2181	East-16	C	90	388	8.13E+00	05:24:13.242	0.114	1.82	0.095	30:41:04.24	0.121	1.7	0.089
2024-01-14T21:18:06.0402	East-16	C	90	602	1.97E+01	05:19:12.118	0.124	3.41	0.073	30:36:22.96	0.132	2.53	0.054
2024-01-15T19:00:19.4148	East-16	C	90	540	1.39E+01	05:14:53.132	0.132	6.5	0.198	30:31:34.70	0.121	5.77	0.176
2024-01-18T18:13:11.6411	East-16	C	90	315	6.58E+00	05:00:27.666	0.129	3	0.194	30:10:42.65	0.109	2	0.129
2024-01-24T19:57:10.129	Draco2	C	90	50	3.68E+00	04:30:27.117	0.187	4	0.461	29:03:09.07	0.149	2.03	0.234
2024-01-30T20:38:56	East-16	C	90	204	1.43E+01	04:01:11.196	0.156	4.42	0.131	27:25:07.81	0.088	2.62	0.078

FIG. 16. Observation log and astrometric measurements for 1991 AQ.

Date + Time	Telescope	Filter	Exp. Time (s)	# Stars Detected	S/N	RA	$\sigma_{\text{sys, RA}}$ [arcsec]	FWHM (RA)	$\sigma_{\text{ran, RA}}$ [arcsec]	Dec	$\sigma_{\text{sys, Dec}}$ [arcsec]	FWHM (Dec)	$\sigma_{\text{ran, Dec}}$ [arcsec]
2024-01-15T18:35:27	West-14	C	15	12	8.11E+01	00:29:24.182	0.195	4.25	0.022	-12:16:49.38	0.190	3.87	0.020
2024-01-18T17:53:30	East-16	C	30	22	8.67E+01	01:15:49.165	0.294	5.84	0.029	-12:47:08.20	0.196	4.11	0.020
2024-01-26T18:22:48	Far-East-20	C	15	23	2.74E+01	03:22:57.303	0.375	4.74	0.073	-11:40:36.73	0.257	5.43	0.084
2024-01-30T20:09:28	East-16	C	30	33	2.24E+02	04:14:52.763	0.103	4.98	0.009	-10:08:27.55	0.186	4.35	0.008
2024-02-07T19:00:43.091	Draco2	C	15	27	6.30E+01	05:25:57.232	0.09	3.23	0.022	-07:02:30.03	0.226	3.11	0.021
2024-02-11T20:32:53.447	West-14	C	15	36	1.34E+02	05:51:06.686	0.101	3.68	0.012	-05:40:27.12	0.119	3.45	0.011
2024-02-18T20:48:03	East-16	C	30	264	1.04E+02	06:24:03.059	0.097	3.75	0.015	-03:41:55.83	0.125	3.38	0.014
2024-02-20T21:47:32.219	Draco2	C	30	116	7.92E+01	06:31:55.281	0.141	4.35	0.023	-03:12:11.14	0.199	4.19	0.022
2024-02-23T19:55:03.615	West-14	C	30	135	1.08E+02	05:42:14.311	0.167	2.86	0.011	-02:32:47.20	0.162	3.21	0.013
2024-02-27T22:11:39.497	Draco2	C	30	179	5.47E+01	06:55:10.090	0.139	4.40	0.034	-01:43:09.33	0.211	3.82	0.030

FIG. 17. Observation log and astrometric measurements for Toro.

Date + Time	Telescope	Filter	Exp. Time (s)	# Stars Detected	S/N	RA	$\sigma_{\text{sys, RA}}$ [arcsec]	FWHM (RA)	$\sigma_{\text{ran, RA}}$ [arcsec]	Dec	$\sigma_{\text{sys, Dec}}$ [arcsec]	FWHM (Dec)	$\sigma_{\text{ran, Dec}}$ [arcsec]
2018-01-29T18:12:56.764	Draco2	C	8	47	3.73E+02	03:58:14.750	0.274	2.66	0.003	28:31:52.43	0.23	2.29	0.003
2018-02-15T18:46:17.062	Draco2	C	8	24	1.88E+00	04:07:53.506	0.462	2.74	0.618	28:36:05.23	0.294	2.66	0.599
2018-02-24T20:37:08.360	Draco2	C	4	4	4.54E-01	04:15:38.899	0.155	3.03	2.831	28:43:47.98	0.003	2.42	2.260
2018-03-07T20:04:24.456	Draco2	C	2	15	1.56E+00	04:27:01.864	0.35	2.45	0.665	28:56:23.52	0.392	2.55	0.692
2018-03-13T20:47:59.114	Draco2	C	15	55	9.09E-01	04:34:05.534	0.246	2.45	1.145	29:04:06.06	0.323	2.45	1.144
2024-02-11T21:58:57	West-14	V	30	10	5.37E+02	11:06:30.736	0.085	3.54	0.003	16:32:02.70	0.055	3.31	0.003
2024-02-12T04:37:50	West-14	V	30	11	5.81E+02	11:06:18.447	0.158	3.8	0.003	16:33:18.42	0.147	4.23	0.003
2024-02-20T22:14:31	Draco2	C	15	10	6.21E+02	10:59:28.440	0.168	5.96	0.004	17:12:17.83	0.193	5.38	0.004
2024-02-23T22:04:12.5402	East-16	V	60	15	3.40E+02	10:56:57.635	0.161	4.7	0.006	17:24:52.52	0.095	3.76	0.005
2024-02-27T22:06:44.140	Draco2	C	8	7	1.49E+00	10:53:31.543	0.174	3.2	0.912	17:40:40.82	0.043	3.02	0.861

FIG. 18. Observation log and astrometric measurements for Dembowska.

Appendix B: Close Approach Distance and Date Histograms

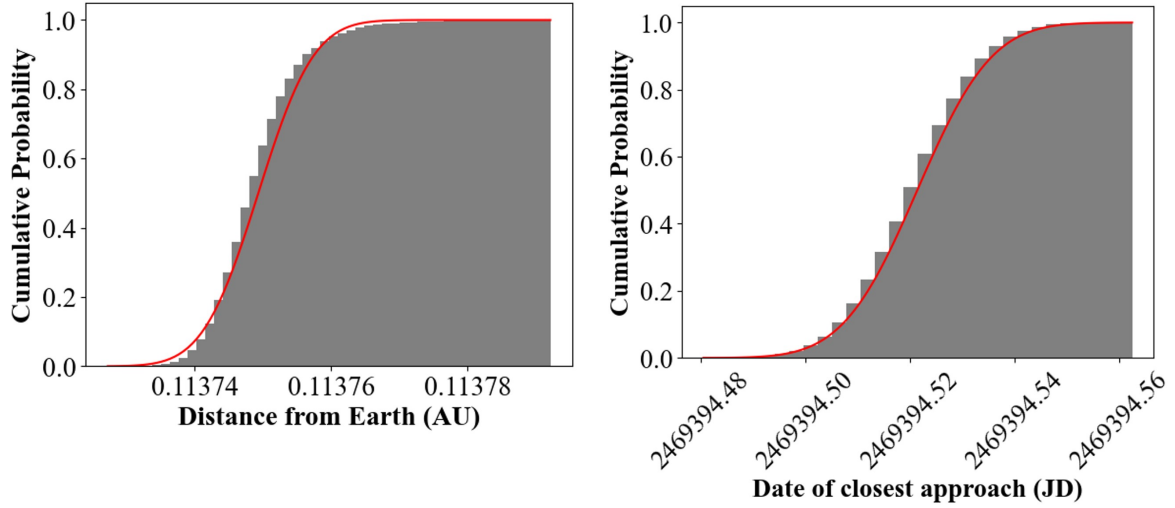


FIG. 19. Cumulative histograms of the close approach distance and date (in Julian Days) for 1998 XB. The cumulative distribution functions are shown in red.

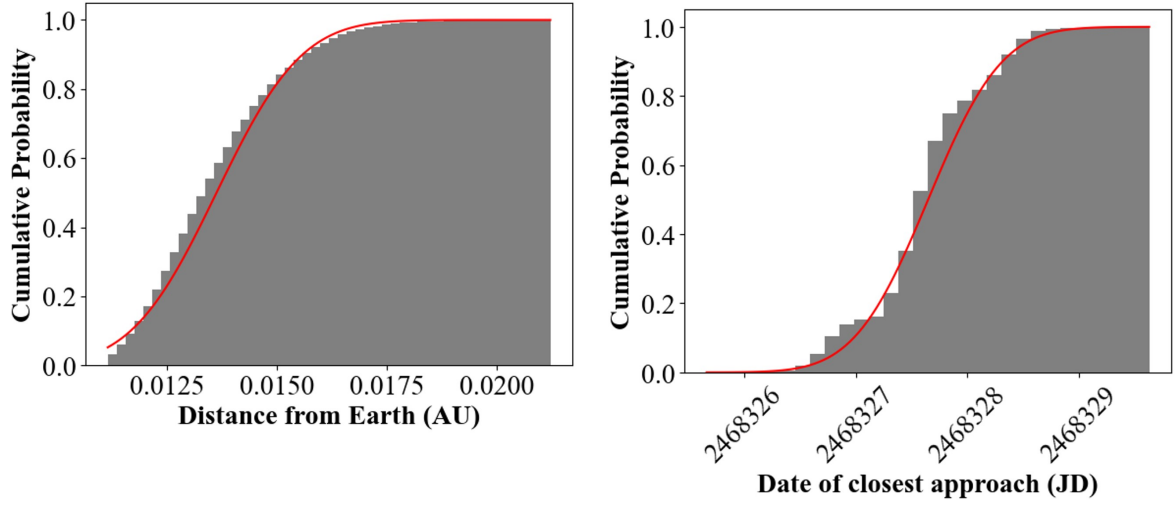


FIG. 20. Cumulative histograms of the close approach distance and date (in Julian Days) for 2001 QQ142. The cumulative distribution functions are shown in red.

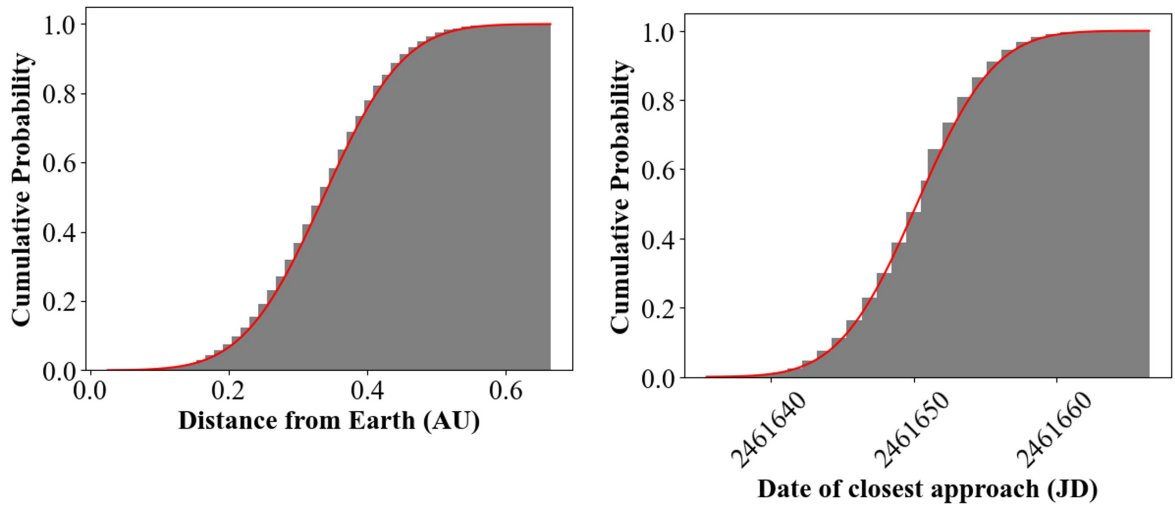


FIG. 21. Cumulative histograms of the close approach distance and date (in Julian Days) for 1991 AQ. The cumulative distribution functions are shown in red.

Appendix C: Error Propagation

There are several quoted uncertainties in this work which were derived by propagating the experimental uncertainties through to the final result. For any error propagation, we use the functional approach. For a multi-variable function, $f(x, y, z)$, where each variable has its own uncertainty ($\alpha_x, \alpha_y, \alpha_z$), the functional uncertainty is given by

$$\alpha_f = \sqrt{(\alpha_f^x)^2 + (\alpha_f^y)^2 + (\alpha_f^z)^2}, \quad (15)$$

where

$$\alpha_f^x = f(x + \alpha_x, y, z) - f(x, y, z), \quad (16)$$

$$\alpha_f^y = f(x, y + \alpha_y, z) - f(x, y, z), \quad (17)$$

and

$$\alpha_f^z = f(x, y, z + \alpha_z) - f(x, y, z). \quad (18)$$

Whilst the above formulae are for a three-variable function, this method is applicable to functions with any number of variables, and hence can be applied to all of the formulae used in this report.